

Tutorial on Silicon Photonics Integrated Platform Fiber Edge Coupling

SERGEY S. AVDEEV^{1,2}, ALEKSANDR S. BABURIN^{1,2}, EVGENIY V. SERGEEV¹, ALEXEI B. KRAMARENKO¹, ARSENIY V. BELYAEV¹, DANIL V. KUSHNEV¹, KIRILL A. BUZAVEROV¹, ILYA A. STEPANOV¹, SERGEY V. BUKATIN¹, ALI SH. AMIRASLANOV¹, EVGENIY S. LOTKOV¹, DMITRIY A. BAKLYKOV¹, AND ILYA A. RODIONOV^{1,2,*}

¹Functional Micro/Nanosystems Research and Educational Center, Bauman Moscow State Technical University, Moscow 105005, Russia

²Dukhov Automatics Research Institute, Moscow 127055, Russia

* Corresponding author: irodionov@bmstu.ru

Abstract: Photonic integrated circuits (PICs) play a crucial role in almost every aspect of modern life, such as data storage, telecommunications, medical diagnostics, green energy, autonomous driving, agriculture, and high-performance computing. To fully harness their benefits, an efficient coupling mechanism is required to successfully launch light into waveguides from fibers. This study introduces low-loss coupling strategies and their implementation for a silicon nitride integrated platform. Here we present an overview of coupling technologies, optimized designs, and a tutorial on manufacturing techniques for inverted tapers, which enable effective coupling for both transverse-magnetic and transverse-electric modes. The optimized coupling losses for the UHNA-7 fiber and the inverted taper Si₃N₄ coupler reached \sim -0.81 dB at 1550 nm per connection for single-mode waveguides with 220×1200 nm cross section. The measured coupling losses in the inverted taper coupler with a standard single-mode fiber were \sim -3.28 dB at 1550 nm per connection for the same platform.

© 2024 Optica Publishing Group under the terms of the [Optica Publishing Group Open Access Publishing Agreement](#)

1. Introduction

With the growing demand for high-speed and compact devices, photonic integrated circuits (PICs) are attracting significant interest because of their high bandwidth and compatibility with large-scale integration technologies. Silicon nitride (Si₃N₄) is the ideal platform for photonic integrated circuit applications such as LiDAR [1], optical sensing [2–5], bio-spectroscopy [6], communication [7] and for uses in the quantum domain, such as quantum key distribution (QKD), quantum computing [8,9] and quantum sensing [10]. In recent years, Si₃N₄ has attracted significant attention as a PIC platform because of its low propagation loss, compatibility with heterogeneous integration, extended transparent bandwidth, and lower susceptibility to errors during the lithography and etching processes compared with the silicon-on-insulator (SOI) platform [11–14]. Typically, PICs require an effective coupling mechanism to launch light into the waveguide from a fiber. To this end, grating and edge couplers are widely employed [15–42]. Grating couplers are used in out-of-plane coupling. For high-volume manufacturing by standard production techniques, for example, in MPW fabs, gratings exhibit a rather low coupling efficiency of \sim -5.0 dB and inherently suffer from limited wavelength bandwidth [15–21]. However, the coupling loss remains relatively high, and the coupling response is polarization dependent. To enhance the coupling efficiency, an inverted taper could be introduced, as it demonstrates a coupling efficiency of up to \sim -0.5 dB [21–24]. However, it should be noted that waveguide type and dimensions and fiber/waveguide mode size differences play a crucial role in coupling efficiency.

Edge couplers exhibit high in-plane light coupling efficiency and a broader spectral bandwidth. Most edge couplers are designed to entail long adiabatic tapers with lengths exceeding several hundred micrometers, thereby enhancing the mode transfer efficiency. Several techniques make it possible to further improve coupling efficiency, like the 2×2 couplers [27–31], mode multiplexers [31–34], and polarization splitters/rotators [35–42]. The compact form of the adiabatic taper drastically facilitates its applicability in high-density PICs [15]. To obtain a short and efficient taper that is applicable in high-density PICs, various taper configurations, including nonlinear, stepwise cascaded, multilayered, and metamaterials, as well as double-tip and sinusoidal taper, have been extensively analyzed for various photonic platforms [19–27]. However, unlike other platforms, compact tapers for Si₃N₄ platform edge couplers have rarely been investigated or reported. The main published results are presented in Table 1.

Table 1. Si₃N₄ taper coupling losses overview

Reference / Wavelength	Taper length / width	Coupling efficiency	3-dB alignment tolerance		Fiber type (mode size)	Waveguide crossection / technology
		TE mode, Losses	Horizontal	Vertical		
[36] Calculated 1550 nm	500 μm / 300 nm	-0.087 dB	±3.6 μm	±3.5 μm	UHNA-3 (4.1±0.3 μm)	100×900 nm / a single step litho
[36] Measured 1550 nm		-0.17 dB	±3.8 μm	±3.6 μm	UHNA-3 (4.1±0.3 μm)	
[34] Measured 1550 nm	500 μm / 180 nm	-2.0 dB	-	-	Lensed polarization-maintaining fibers (LPMFs) (2.5±0.3 μm)	400×700 nm / polished with diamond films
[38] Calculated 1550 nm	45 μm / 750 nm	-0.58 dB	±1.0 μm	±1.0 μm	UHNA-3 (4.1±0.3 μm)	300×1000 nm / shadow mask
[38] Measured 1550 nm		-1.47 dB	-	-		
[43] Calculated 1550 nm	76 μm / 200 nm	-0.29 dB	±2.0 μm	±2.0 μm	UHNA-3 (4.1±0.3 μm)	500×2000 nm / a single step litho
[43] Measured 1550 nm		-0.36 dB	±3.5 μm	±3.3 μm		
Current work Calculated 1550 nm	360 μm / 275 nm	-2.52 dB	± 3.2 μm	± 2.9 μm	SMF-28 (10.5±0.5 μm)	220×1200 nm / double step
	360 μm / 275 nm	-1.55 dB	± 2.0 μm	± 1.5 μm	SM1500es (4.0±0.5 μm)	
	360 μm / 275 nm	-0.75 dB	± 1.7 μm	± 1.3 μm	UHNA-7 (3.2±0.3 μm)	
	360 μm / 275 nm	-0.55 dB	± 1.5 μm	± 1.2 μm	LPMFs (2.5±0.3 μm)	
Current work Measured 1550 nm	360 μm / 275 nm	-3.28 dB	± 2.8 μm	± 2.4 μm	SMF-28 (10.5±0.5 μm)	
	360 μm / 275 nm	-1.25 dB	± 1.4 μm	± 1.1 μm	SM1500es (4±0.5 μm)	
	360 μm / 275 nm	-0.81 dB	± 1.2 μm	± 0.8 μm	UHNA-7 (3.2±0.3 μm)	
	360 μm / 275 nm	-0.97 dB	± 0.9 μm	± 0.7 μm	LPMFs (2.5±0.3 μm)	

Currently, the best achieved efficiency of -0.17 dB was demonstrated by the adiabatic Si₃N₄ coupler based on a taper with a length of 500 μm for UHNA-3 fiber/100×900 nm waveguide interface, cleaved with a good cleaving position tolerance [36].

This paper serves as a tutorial on finding the best repeatable wafer-scale compatible coupling strategy for the Si₃N₄ platform. First, the entire Si₃N₄ waveguide fabrication process is discussed. It comprises waveguide fabrication and plasma dicing based on deep silicon etching, which provides optical quality chip edge forming. Then, a universal approach for taper design is presented, which was used to simulate several types of inverted taper couplers. The coupling losses per coupler for the lensed fiber/chip coupling are calculated to be ~-0.55 dB and measured to be ~-1.25 dB for 1550 nm per connection; for standard fiber/chip coupling are calculated to be ~-2.52 dB and measured to be ~-3.28 dB for 1550 nm per connection.

2. Coupling strategies

2.1 Tapered waveguide simulation

For PICs, low-loss edge coupling special waveguide structures, which serve as mode size converters, are used [44,45]. The optical mode size and shape change during propagation through the tapered waveguide to achieve higher coupling efficiency between two modes with different cross-sections. They are designed to operate adiabatically: the waveguide local first-order mode should propagate through the tapered waveguide while undergoing relatively little mode conversion compared with the higher-order modes or radiation modes. This adiabatic operation is realized in the taper design by gradually increasing the taper cross-section size and decreasing the mode size from typical diameter of 5-10 μm in fiber to the order of several microns in the waveguide. Different designs of adiabatic tapers have been proposed for Si₃N₄ platforms, including linear [44], exponential [20], parabolic [46], and multi-sectional tapers [22,23]. Most often, a linear waveguide taper was used. In this linear adiabatic taper mode, conversion occurs more easily in the wider portion [20]. For low-loss transmission, the linear taper can be extended to be long enough to ensure adiabatic propagation. However, a longer taper could lead to higher propagation losses. This problem becomes more critical when the two modes connected by the linear taper possess higher cross-sectional differences. In this case, the taper starts with a width that is much narrower than that of the waveguide. This makes the taper wall roughness' influence on losses much more noticeable. Thus, the taper length should be reduced to ensure the lowest probable losses and to reduce the device footprint. To determine the geometry of the waveguide in which only fundamental modes will be excited (Fig. 2a), modeling was carried out in Ansys Lumerical FDE, on the basis of which a waveguide width of 1200 nm was chosen. To determine the optimal taper geometry, modeling was performed in Ansys Lumerical FDTD based on the numerical solution of Maxwell's equations. The taper 3D model is shown in Fig. 1a.

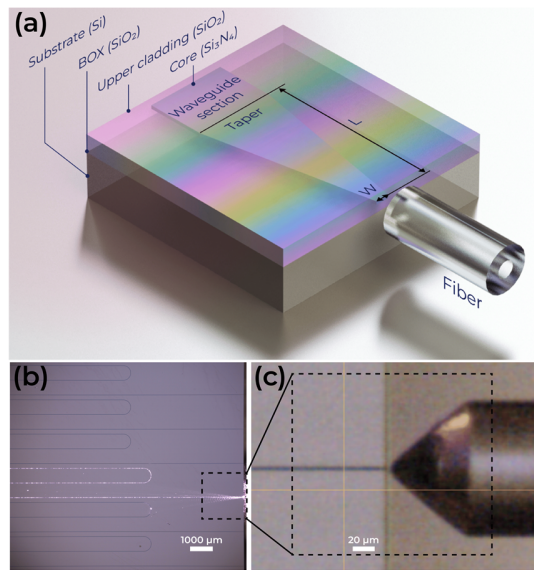


Fig. 1. 3D visualization of coupled taper with fiber (a), Light propagation through the waveguide (b), Coupling of lensed fiber with chip facet (c).

The length of the taper varied from 200 μm to 520 μm , which was determined by the size of the chip (Fig. 2 (c-f)). In turn, the width at the beginning of the taper varied from 50 to 500 nm with a waveguide width of 1200 nm. The lower limit of this range is due to the technological capabilities of electron lithography. The graph shows the dependence obtained during the simulation for different optical fibers. In this study, the taper length was 360 μm for high transmission maintaining a relatively small device footprint. To standardize the technological process, a taper geometry (width 280 nm, length 360 μm) was chosen to ensure maximum coupling efficiency for all types of optical fibers. The light was emitted from the fiber onto the mode size converter, as shown in the top-down view in Fig. 2h.

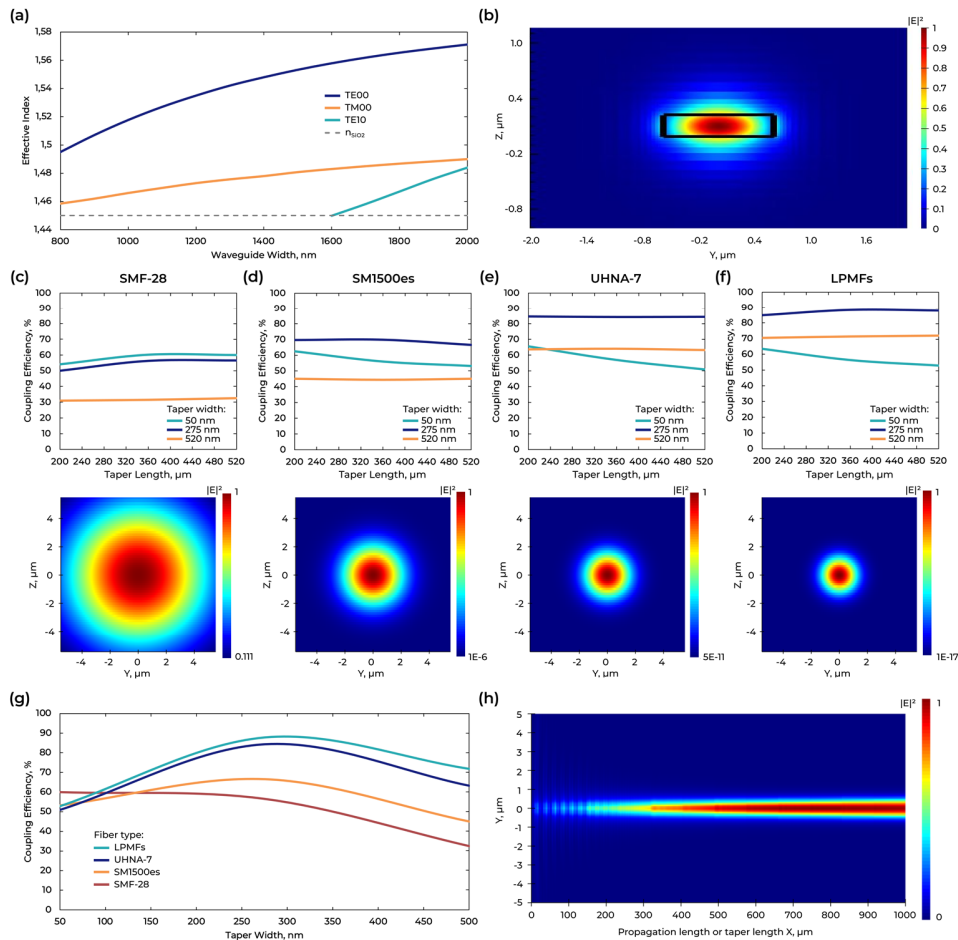


Fig. 2. Calculation of Si₃N₄ effective index of modes excited in a waveguide as a function of waveguide width (a), Fundamental mode excited in the waveguide with 220×1200 nm cross section (b), Calculation of the taper length at different width for different fiber types with wavelength 1550 nm (c-f), Calculation of the taper width with fixed length of taper (360 μm) for different fiber types with wavelength 1550 nm (g) and simulation of mode propagation for lensed fiber (h).

2.2 Edge facet

To provide high taper coupling efficiency, the PIC dies are typically polished to obtain high optical grade quality edges [47]. Although this process works well with small volumes, its scaling up to wafer level is impractical. There is also used the process of wet etching of thick layers of silicon dioxide, but it is anisotropic, that negatively affects the quality of the optical facets [48]. Other solutions for PICs optical facets fabrication need to be investigated. A promising technology is the reactive plasma dicing [49].

We previously demonstrated the lowest propagation losses currently available in the near-infrared wavelength (as low as 0.55 dB/cm) in single-mode Si₃N₄ submicron waveguides (220×550 nm) [50]. Our study continues the previous research and presents a plasma-based process for optical grade edge facets fabrication. The fabrication process of low-loss silicon nitride photonic integrated circuits with light coupling through edge couplers is shown in Fig. 3. The presented technology is used to dice a 220-nm-thick stoichiometric low-pressure chemical

vapor Si_3N_4 layer grown on the 525- μm silicon substrate oxidized with the 2.5- μm thickness and covered with 2.5- μm oxide. A standard sequence of basic operations is involved for fabrication (Fig. 3). First, the waveguide structure alignment markers were patterned using electron-beam lithography. The pattern is then transferred to the Si_3N_4 device layer by reactive ion plasma etching (RIE) [51]. After nanotopology fabrication, the chip is plasma diced. The dicing process consists of the following stages: surface preparation, photoresist spin coating, photolithography, photoresist development, $\text{SiO}_2\text{-Si}_3\text{N}_4\text{-SiO}_2$ thin film stack etching, photoresist removal, and silicon etching by the Bosch technique [51].

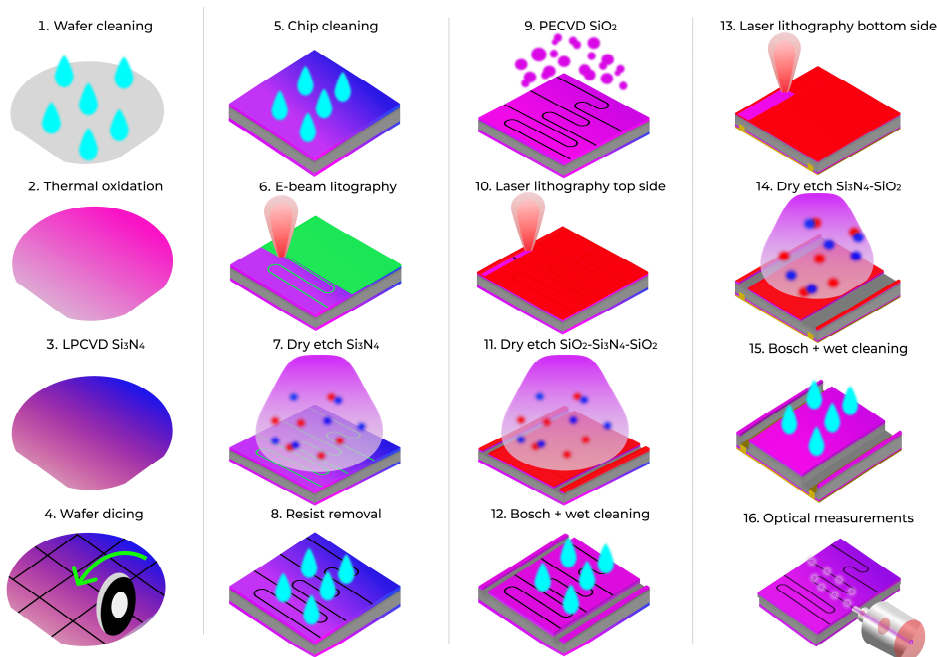


Fig. 3. Si_3N_4 PICs with edge coupling fabrication process.

To pattern the silicon dioxide layer, 5 μm thick SPR220 photoresist was used. Patterning processes were performed using laser lithography. The topology was then transferred to the multilayer stack ($\text{SiO}_2\text{-Si}_3\text{N}_4\text{-SiO}_2$) the with reactive ion etching. The next step was silicon wafer dicing using the Bosch process. Optical microscopy and scanning electron microscopy were used to characterize the samples and control process quality.

The mentioned above SPR220 positive photoresist pattern transfer mask with an anti-reflective layer using laser lithography should have a vertical profile to be further used for vertical edge etching. It lets avoiding the effect of refraction during light coupling from the optical fibers to the chip. Resist thickness was chosen based on plasma etching process selectivity to ensure etching of $\text{SiO}_2\text{-Si}_3\text{N}_4\text{-SiO}_2$ layers with a total thickness of 5.2 μm . The laser lithography dose and focus were varied to obtain the pattern mask vertical profile. for the structural vertical angle exposure in thick resist layers, multi-pass lithography was used [52]. In this study, four- and six- pass algorithms were applied (Fig. 4b).

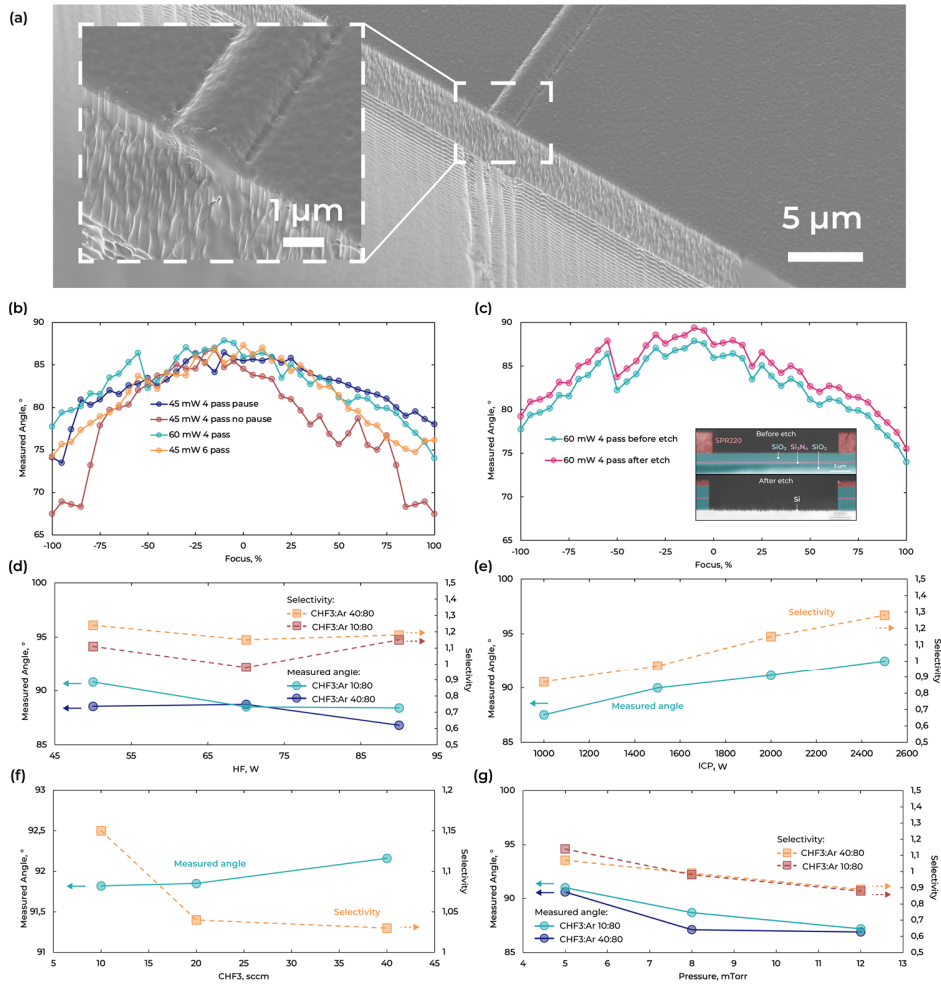


Fig. 4. SEM image of the fabricated edge coupler (a), dependance of the resist sidewall angle on the laser lithography power and focus value (b), sidewall angle comparison before and after etching (c), SiO₂-Si₃N₄-SiO₂ layers sidewall angle and selectivity dependance on gas mixture (d), SiO₂-Si₃N₄-SiO₂ layers sidewall angle and selectivity dependance on ICP power (e), SiO₂-Si₃N₄-SiO₂ layers sidewall angle and selectivity dependance on CHF₃ amount (f) and SiO₂-Si₃N₄-SiO₂ layers sidewall angle and selectivity dependance on chamber pressure (g).

A clear maximum can be seen in Fig. 5b. The 88.7° resist sidewall angle corresponds to the following lithography regime: 60 mW laser power, 4 passes, -15 % focus. The found regime was further used in etching technology development.

Etching was performed using the ICP-RIE system. For etching thick layers of silicon dioxide (more than 5 μm) with a vertical profile (90±0.5°) and a smooth edge surface, the CHF₃ process gas was selected. During etching process, the CF_x polymer film is deposited on the side walls during the etch process and protects the side surface, simultaneously providing a vertical profile [53,54]. In addition, Ar was added to the plasma to stimulate the etching process.

An increase in the plasma power source in the CHF₃/Ar plasma mixture from 1000 W to 2500 W led to an increase in selectivity from 0.9 to 1.3 due to a decrease in the bias voltage due to the increase in plasma volume. At the same time, the profile angle increased in the

positive direction from 88.7° to 92.5° because of the growth of radicals and, as a result, of the process chemical components [55].

An increase in stage power in the range from 50 to 90 W leads to an increase in the bias voltage and an increase in the ionic etching component, which results in a general decrease in selectivity with the local minimum observed at 70 W. With an increase in the process ionic component, the profile angle narrows toward anisotropy (from 88.5° to 86.5°), which, along with the ICP source, is a fairly effective tool for controlling both selectivity and profile angle.

A decrease in the working pressure reduces the total number of collisions within the plasma mixture, thereby increasing the overall direction of the mixture toward the substrate. Through such effects, the profile angle became more negative, and the overall selectivity was reduced because of the presence of more energetic ions in the mixture composition [55].

Increasing the amount of the main etching gas CHF₃ in the mixture (from 10 sccm to 40 sccm) did not significantly affect the overall process dynamics in terms of the profile angle and remains in the range of 91.85° to 92.15°, which could be considered insignificant. However, a significant increase in the etch rate (from 150 nm/min to 230 nm/min) and a slight decrease in selectivity (from 1.15 to 1.03) were observed. Profile angle preservation with an increase in the etching rate could be associated with preservation of the passivation/etching balance on the channel side walls and simultaneous increase in the ionic and fluorine radicals [56].

Based on the obtained equations, the following etching regime was chosen: stage power 50 W, ICP power 2000 W, pressure 5 mTorr, CHF₃ flow 40 sccm, and Ar flow 80 sccm.

3. Characterization

3.1. Cut-back measurement

To measure the I/O efficiency, an automated assembly system equipped with a 5-nm resolution 12-axis alignment drive, 935 nm and 1550 nm wavelength laser sources, and an optical power meter was used. This system made it possible to measure internal optical losses and coupling efficiency using the output power values of structures of various lengths.

The cut-back propagation loss analysis [57,58] in the fabricated Si₃N₄ waveguides was performed for an integrated circuit, and light was coupled out with the angled polished FAU to power the detector. Propagation losses were measured on the test photonic integrated circuits with varying length structures for loss measurement and are shown in Fig. 5a.

Fig. 5b presents the measured coupling losses for different fiber type. The lowest losses of about -0.81 dB are observed for UHNA-7 fiber. To characterize propagation losses more accurate optical frequency domain reflectometry (OFDR) was used.

3.2. OFDR measurements

Reflectometry is widely used in fiber optics to probe the local reflectivity of waveguides and devices with respect to propagation distance [59]. With a point-to-point resolution of about 10 μm and detection sensitivity of -130 dB over 30 m of propagation, coherent optical backscattering reflectometry (OFDR) is a particularly useful technique in characterizing waveguides and devices at the planar scale [60,61]. In the OFDR, a continuous wave laser source is scanned over several terahertz in frequency or, equivalently, several tens of nanometers in wavelength. A larger scan range improves the measurement spatial resolution according to the following expression:

$$D_{min} \cong \frac{c}{2n_g|f_{start}-f_{end}|} = \frac{\lambda_{start}\lambda_{end}}{2n_g|\lambda_{start}-\lambda_{end}|}, \quad (1)$$

where: D_{min} is the minimum distance between the two data points, c is the speed of light, n_g is the group index, f_{start} and λ_{start} are the source frequency and wavelength at the scanning start, respectively, and f_{end} and λ_{end} are the source frequency and wavelength at the scanning end

[62]. However, all parameters derived from the spatial domain data are then averaged over the measurement scan spectral range. If the parameter spectral dependence is set, the rectangular window function can be applied to data in the spectral domain to narrow the included spectral range. This window could be moved across the measurement's full spectral range, making it possible to extract the parameter at each window position and obtain the parameter spectral dependence from a single OFDR scan. Because narrowing data in the frequency domain decreases the measurement spatial resolution according to Eq. (2), a tradeoff appears between the spectral averaging, which could distort the actual spectral dependence and the measurement accuracy. In this study, a window width of 10 nm is used to extract the spectrally dependent measurements of the group index, coupling loss, critical bend radius, and propagation loss.

Figure 5d shows the OFDR data from two UHNA-7 fibers coupled to waveguides (10 cm long). The data was not filtered in the spectral domain, and a moving average filter with 100-datapoint or ~1 mm window size was applied in the spatial domain to reduce the backscatter amplitude deviation. Before OFDR scanning, fiber-to-chip coupling was maximized using an OFDR source laser and an optical power meter. The dashed lines in Fig. 5d indicate the mean backscatter levels in waveguide. The difference between these two levels of 5.96 dB includes the total return loss between the two fibers, or:

$$RL_{dB}^{total} = 2IL_{dB}^{total} = 2(IL_{dB}^{fiber-to-chip} + IL_{dB}^{propagation} + IL_{dB}^{fiber-to-chip}), \quad (2)$$

where: RL_{dB}^{total} is the total return loss in dB, IL_{dB}^{total} is the total insertion loss, fiber-to-chip IL_{dB} is the fiber-to-chip insertion loss per facet, and propagation IL_{dB} is the total propagation insertion loss.

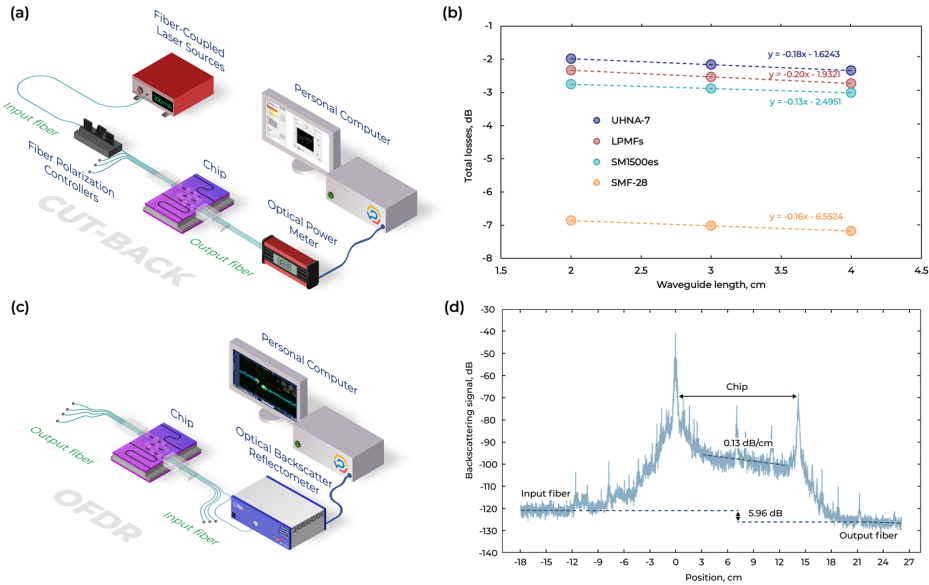


Fig. 5. Schematic of the measurement setup for cut-back characterization (a); Propagation losses measured by the cut-back calculated: $y = k \times x + b$; $k = \text{propagation losses}$, $b = \text{coupling losses}$ for wavelength 1550 nm (b); Schematic of the measurement setup for OFDR characterization (c) and OFDR characterization along the waveguide. The dashed line shows the linear fit of the waveguide reflections (d)

The measured data is linearly fitted to find propagation losses (Fig. 5d). Based on OFDR characterization, the propagation insertion loss is 0.13 dB/cm and fiber-to-chip insertion loss per facet is 0.84 dB.

4. Conclusion

This study presents a universal strategy for repeatable wafer-scale PIC low-loss edge coupling. For a coupling platform, we present a tutorial on the design, manufacturing, and characterization of lithographically defined optical coupling facets using an ICP dry etching technique. Manufacture process optimization allowed us to obtain the 89 degrees optical grade facet that provides coupling losses lower than 1 dB for a wide range of optical fibers that agrees well with the simulation. To reduce propagation insertion losses, fabrication process should include chemical-mechanical polishing and long-term annealing steps. We believe that this research would be useful for a wide PIC community.

Acknowledgments

Samples were fabricated and measured at the BMSTU Nanofabrication Facility (FMN Laboratory, FMNS REC, ID 74300)

Disclosures

The authors declare no conflicts of interest.

Data availability

Data that support the findings of this study are available from the corresponding author upon a reasonable request.

References

1. S. Malhouitre, D. Fowler, S. Garcia, O. Lemonnier, N. Tyler, and W. Rabaud, "Silicon Nitride Photonic Platform for LIDAR Applications," in *2018 IEEE 15th International Conference on Group IV Photonics (GFP)* (2018), pp. 1–2.
2. A. S. Baburin, A. Ivanov, I. Trofimov, A. Dobronosova, P. Melentiev, V. Balykin, D. Moskalev, A. Pishchimova, L. Ganieva, I. Ryzhikov, and I. Rodionov, "Highly directional plasmonic nanolaser based on high-performance noble metal film photonic crystal," in *(SPIE-Intl Soc Optical Eng, 2018)*, p. 159.
3. G. M. Yankovskii, A. V. Komarov, R. S. Puz'ko, A. V. Baryshev, K. N. Afanas'ev, I. A. Boginskaya, I. V. Bykov, A. M. Merzlikin, I. A. Rodionov, and I. A. Ryzhikov, "Structural and optical properties of single and bilayer silver and gold films," *Physics of the Solid State* **58**(12), 2503–2510 (2016).
4. A. S. Baburin, A. I. Ivanov, I. A. Ryzhikov, I. V. Trofimov, A. R. Gabidullin, D. O. Moskalev, Y. V. Panfilov, and I. A. Rodionov, "Crystalline structure dependence on optical properties of silver thin film over time," in *2017 Progress In Electromagnetics Research Symposium - Spring (PIERS)* (2017), pp. 1497–1502.
5. A. S. Baburin, D. O. Moskalev, E. S. Lotkov, O. S. Sorokina, D. A. Baklykov, S. S. Avdeev, K. A. Buzaverov, G. M. Yankovskii, A. V. Baryshev, I. A. Ryzhikov, and I. A. Rodionov, "Evolutionary selection growth of silver films for low-loss nanophotonic devices," *Surfaces and Interfaces* **39**, 102897 (2023).
6. H. Hoi, S. S. Rezaie, L. Gong, P. Sen, H. Zeng, C. Montemagno, and M. Gupta, "Biofunctionalized silicon nitride platform for sensing applications," *Biosens Bioelectron* **102**, 497–503 (2018).
7. E. S. Lotkov, A. S. Baburin, I. A. Ryzhikov, O. S. Sorokina, A. I. Ivanov, A. V. Zverev, V. V. Ryzhkov, I. V. Bykov, A. V. Baryshev, Y. V. Panfilov, and I. A. Rodionov, "ITO film stack engineering for low-loss silicon optical modulators," *Sci Rep* **12**(1), (2022).
8. C. Taballione, T. A. W. Wolterink, J. Lugani, A. Eckstein, B. A. Bell, R. Grootjans, I. Visscher, D. Geskus, C. G. H. Roeloffzen, J. J. Renema, I. A. Walmsley, P. W. H. Pinkse, and K.-J. Boller, "8x8 reconfigurable quantum photonic processor based on silicon nitride waveguides," *Opt Express* **27**(19), 26842 (2019).
9. I. A. Stepanov, A. S. Baburin, D. V. Kushnev, E. V. Sergeev, O. I. Shmonina, A. R. Matanin, V. V. Echeistov, I. A. Ryzhikov, Y. V. Panfilov, and I. A. Rodionov, "Sputtered NbN films for ultrahigh performance superconducting nanowire single-photon detectors," *APL Mater* **12**(2), (2024).
10. H.-C. Weng, J. Monroy-Ruz, J. C. F. Matthews, J. G. Rarity, K. C. Balram, and J. A. Smith, "Heterogeneous Integration of Solid-State Quantum Systems with a Foundry Photonics Platform," *ACS Photonics* **10**(9), 3302–3309 (2023).
11. C. Xiang, W. Jin, and J. E. Bowers, "Silicon nitride passive and active photonic integrated circuits: trends and prospects," *Photonics Res* **10**(6), A82 (2022).
12. X. Guo, X. Ji, B. Yao, T. Tan, A. Chu, O. Westreich, A. Dutt, C. Wong, and Y. Su, "Ultra-wideband integrated photonic devices on silicon platform: from visible to mid-IR," *Nanophotonics* **12**(2), 167–196 (2023).
13. R. Baets, A. Z. Subramanian, S. Clemmen, B. Kuyken, P. Bienstman, N. Le Thomas, G. Roelkens, D. Van Thourhout, P. Helin, and S. Severi, "Silicon Photonics: silicon nitride versus silicon-on-insulator," in *Optical Fiber Communication Conference (OSA, 2016)*, p. Th3J.1
14. P. Muñoz, G. Micó, L. Bru, D. Pastor, D. Pérez, J. Doménech, J. Fernández, R. Baños, B. Gargallo, R. Alemany, A. Sánchez, J. Cirera, R. Mas, and C. Domínguez, "Silicon Nitride Photonic Integration Platforms for Visible, Near-Infrared and Mid-Infrared Applications," *Sensors* **17**(9), 2088 (2017).
15. B. Ben Bakir, A. V. de Gyves, R. Orobtcchouk, P. Lyan, C. Porzier, A. Roman, and J.-M. Fedeli, "Low-Loss (<1 dB) and Polarization-Insensitive Edge Fiber Couplers Fabricated

- on 200-mm Silicon-on-Insulator Wafers," *IEEE Photonics Technology Letters* 22(11), 739–741 (2010).
16. N. Hatori, T. Shimizu, M. Okano, M. Ishizaka, T. Yamamoto, Y. Urino, M. Mori, T. Nakamura, and Y. Arakawa, "A Hybrid Integrated Light Source on a Silicon Platform Using a Trident Spot-Size Converter," *Journal of Lightwave Technology* 32(7), 1329–1336 (2014).
 17. Y. Urino, T. Usuki, J. Fujikata, M. Ishizaka, K. Yamada, T. Horikawa, T. Nakamura, and Y. Arakawa, "High-density and wide-bandwidth optical interconnects with silicon optical interposers [Invited]," *Photonics Res* 2(3), A1 (2014).
 18. P. Cheben, J. H. Schmid, S. Wang, D.-X. Xu, M. Vachon, S. Janz, J. Lapointe, Y. Painchaud, and M.-J. Picard, "Broadband polarization independent nanophotonic coupler for silicon waveguides with ultra-high efficiency," *Opt Express* 23(17), 22553 (2015).
 19. M. Papes, P. Cheben, D. Benedikovic, J. H. Schmid, J. Pond, R. Halir, A. Ortega-Moñux, G. Wangüemert-Pérez, W. N. Ye, D.-X. Xu, S. Janz, M. Dado, and V. Vašinek, "Fiber-chip edge coupler with large mode size for silicon photonic wire waveguides," *Opt Express* 24(5), 5026 (2016).
 20. Y. Atsumi, T. Yoshida, E. Omoda, and Y. Sakakibara, "Broad-band surface optical coupler based on a SiO₂-capped vertically curved silicon waveguide," *Opt Express* 26(8), 10400 (2018).
 21. T. Shoji, T. Tsuchizawa, T. Watanabe, K. Yamada, and H. Morita, "Low loss mode size converter from 0.3 μ m square Si wire waveguides to singlemode fibres," *Electron Lett* 38(25), 1669 (2002).
 22. V. R. Almeida, R. R. Panepucci, and M. Lipson, "Nanotaper for compact mode conversion," *Opt Lett* 28(15), 1302 (2003).
 23. G. Roelkens, P. Dumon, W. Bogaerts, D. Van Thourhout, and R. Baets, "Efficient silicon-on-insulator fiber coupler fabricated using 248-nm-deep UV lithography," *IEEE Photonics Technology Letters* 17(12), 2613–2615 (2005).
 24. S. McNab, N. Moll, and Y. Vlasov, "Ultra-low loss photonic integrated circuit with membrane-type photonic crystal waveguides," *Opt Express* 11(22), 2927 (2003).
 25. R. Marchetti, C. Lacava, L. Carroll, K. Gradkowski, and P. Minzioni, "Coupling strategies for silicon photonics integrated chips [Invited]," *Photonics Res* 7(2), 201 (2019).
 26. Y. Zhu, J. Wang, W. Xie, B. Tian, Y. Li, E. Brainis, Y. Jiao, and D. Van Thourhout, "Ultra-compact silicon nitride grating coupler for microscopy systems," *Opt Express* 25(26), 33297 (2017).
 27. J. C. C. Mak, W. D. Sacher, H. Ying, X. Luo, P. G.-Q. Lo, and J. K. S. Poon, "Multi-layer silicon nitride-on-silicon polarization-independent grating couplers," *Opt Express* 26(23), 30623 (2018).
 28. G. Son, S. Han, J. Park, K. Kwon, and K. Yu, "High-efficiency broadband light coupling between optical fibers and photonic integrated circuits," *Nanophotonics* 7(12), 1845–1864 (2018).
 29. O. Mitomi, K. Kasaya, and H. Miyazawa, "Design of a single-mode tapered waveguide for low-loss chip-to-fiber coupling," *IEEE J Quantum Electron* 30(8), 1787–1793 (1994).
 30. J. Zou, Y. Yu, M. Ye, L. Liu, S. Deng, X. Xu, and X. Zhang, "Short and efficient mode-size converter designed by segmented-stepwise method," *Opt Lett* 39(21), 6273 (2014).
 31. T. Mizuno, T. Kitoh, M. Ishii, Y. Inoue, T. Saida, M. Itoh, T. Shibata, and Y. Hibino, "Compact and low-loss arrayed waveguide grating module with tolerance-relaxed spot-size converter," *IEEE Photonics Technology Letters* 15(2), 239–241 (2003).
 32. P. Cheben, J. H. Schmid, S. Wang, D.-X. Xu, M. Vachon, S. Janz, J. Lapointe, Y. Painchaud, and M.-J. Picard, "Broadband polarization independent nanophotonic coupler for silicon waveguides with ultra-high efficiency," *Opt Express* 23(17), 22553 (2015).

33. Y. Liu, W. Sun, H. Xie, N. Zhang, K. Xu, Y. Yao, S. Xiao, and Q. Song, "Adiabatic and Ultracompact Waveguide Tapers Based on Digital Metamaterials," *IEEE Journal of Selected Topics in Quantum Electronics* 25(3), 1–6 (2019).
34. H. Tao, J. Song, Q. Fang, M. Yu, G. Lo, and D. Kwong, "Improving coupling efficiency of fiber-waveguide coupling with a double-tip coupler," *Opt Express* 16(25), 20803 (2008).
35. N. Kohli, M. Ménard, and W. N. Ye, "Efficient TE/TM spot-size converter for broadband coupling to single mode fibers," *OSA Contin* 2(8), 2428 (2019).
36. T. Zhu, Y. Hu, P. Gatkine, S. Veilleux, J. Bland-Hawthorn, and M. Dagenais, "Ultrabroadband High Coupling Efficiency Fiber-to-Waveguide Coupler Using Si₃N₄/SiO₂ Waveguides on Silicon," *IEEE Photonics J* 8(5), 1–12 (2016).
37. P. Sethi, R. Kallega, A. Haldar, and S. K. Selvaraja, "Compact broadband low-loss taper for coupling to a silicon nitride photonic wire," *Opt Lett* 43(14), 3433 (2018).
38. J. Fernández, R. Baños, D. Doménech, C. Domínguez, and P. Muñoz, "Low-loss inverted taper edge coupler in silicon nitride," *IET Optoelectronics* 13(2), 62–66 (2019).
39. Y. Wang, L. Xu, H. Yun, M. Ma, A. Kumar, E. El-Fiky, R. Li, N. Abadiacalvo, L. Chrostowski, N. A. F. Jaeger, and D. V. Plant, "Polarization-Independent Mode-Evolution-Based Coupler for the Silicon-on-Insulator Platform," *IEEE Photonics J* 10(3), 1–10 (2018).
40. L. Xu, Y. Wang, A. Kumar, E. El-Fiky, D. Mao, H. Tamazin, M. Jacques, Z. Xing, Md. G. Saber, and D. V. Plant, "Compact high-performance adiabatic 3-dB coupler enabled by subwavelength grating slot in the silicon-on-insulator platform," *Opt Express* 26(23), 29873 (2018).
41. H. Yun, L. Chrostowski, and N. A. F. Jaeger, "Ultra-broadband 2 × 2 adiabatic 3 dB coupler using subwavelength-grating-assisted silicon-on-insulator strip waveguides," *Opt Lett* 43(8), 1935 (2018).
42. D. Mao, M. S. Alam, J. Zhang, M. Zhu, P.-C. Koh, D. V. Plant, Y. Wang, E. El-Fiky, L. Xu, A. Kumar, M. Jaques, A. Samani, O. Carpentier, and S. Bernal, "Adiabatic Coupler With Design-Intended Splitting Ratio," *Journal of Lightwave Technology* 37(24), 6147–6155 (2019).
43. B. Bhandari, C.-S. Im, K.-P. Lee, S.-M. Kim, M.-C. Oh, and S.-S. Lee, "Compact and Broadband Edge Coupler Based on Multi-Stage Silicon Nitride Tapers," *IEEE Photonics J* 12(6), 1–11 (2020).
44. Y. Fu, T. Ye, W. Tang, and T. Chu, "Efficient adiabatic silicon-on-insulator waveguide taper," *Photonics Res* 2(3), A41 (2014).
45. M. Pu, L. Liu, H. Ou, K. Yvind, and J. M. Hvam, "Ultra-low-loss inverted taper coupler for silicon-on-insulator ridge waveguide," *Opt Commun* 283(19), 3678–3682 (2010).
46. S. J. Hettrick, J. Wang, C. Li, J. S. Wilkinson, and D. P. Shepherd, "An Experimental Comparison of Linear and Parabolic Tapered Waveguide Lasers and a Demonstration of Broad-Stripe Diode Pumping," *Journal of Lightwave Technology* 22(3), 845–849 (2004).
47. J. M. Fedeli, R. Orobitchouk, C. Seassal, and L. Vivien, "Integration issues of a photonic layer on top of a CMOS circuit," in J. A. Kubby and G. T. Reed, eds. (2006), p. 61250H.
48. T. G. Konstantinova, M. M. Andronic, D. A. Baklykov, V. E. Stukalova, D. A. Ezenkova, E. V. Zikiy, M. V. Bashinova, A. A. Solovev, E. S. Lotkov, I. A. Ryzhikov, and I. A. Rodionov, "Deep multilevel wet etching of fused silica glass microstructures in BOE solution," *Sci Rep* 13(1), (2023).
49. M. Schnarrenberger, L. Zimmermann, T. Mitze, J. Bruns, and K. Petermann, "Facet preparation of SOI waveguides by etching and cleaving compared to dicing and polishing," in 2004 10th International Workshop on Computational Electronics (IEEE Cat. No.04EX915) (IEEE, n.d.), pp. 72–74.
50. K. A. Buzaverov, A. S. Baburin, E. V. Sergeev, S. S. Avdeev, E. S. Lotkov, M. Andronik, V. E. Stukalova, D. A. Baklykov, I. V. Dyakonov, N. N. Skryabin, M. Yu.

- Saygin, S. P. Kulik, I. A. Ryzhikov, and I. A. Rodionov, "Low-loss silicon nitride photonic ICs for near-infrared wavelength bandwidth," *Opt Express* 31(10), 16227 (2023).
51. D. A. Baklykov, M. Andronic, O. S. Sorokina, S. S. Avdeev, K. A. Buzaverov, I. A. Ryzhikov, and I. A. Rodionov, "Self-Controlled Cleaving Method for Silicon DRIE Process Cross-Section Characterization," *Micromachines (Basel)* 12(5), 534 (2021).
 52. M. R. Haq and H. Schiff, "Vertical sidewalls in thick epoxy resists – a challenge for laser-based direct write lithography," *Micro and Nano Engineering* 19, 100210 (2023).
 53. S. Hayashi, M. Yamanaka, H. Nakagawa, M. Kubota, and M. Ogura, "SiO₂ etching using inductively coupled plasma," *Electronics and Communications in Japan (Part II: Electronics)* 81(9), 21–29 (1998).
 54. G. S. Oehrlein, Y. Zhang, D. Vender, and O. Joubert, "Fluorocarbon high-density plasmas. II. Silicon dioxide and silicon etching using CF₄ and CHF₃," *Journal of Vacuum Science & Technology A: Vacuum, Surfaces, and Films* 12(2), 333–344 (1994).
 55. F. Gaboriau, G. Cartry, M.-C. Peignon, and Ch. Cardinaud, "Selective and deep plasma etching of SiO₂: Comparison between different fluorocarbon gases (CF₄, C₂F₆, CHF₃) mixed with CH₄ or H₂ and influence of the residence time," *Journal of Vacuum Science & Technology B: Microelectronics and Nanometer Structures Processing, Measurement, and Phenomena* 20(4), 1514–1521 (2002).
 56. B. Kim, K.-H. Kwon, S.-K. Kwon, J.-M. Park, S. W. Yoo, K.-S. Park, I.-K. You, and B.-W. Kim, "Modeling etch rate and uniformity of oxide via etching in a CHF₃/CF₄ plasma using neural networks," *Thin Solid Films* 426(1–2), 8–15 (2003).
 57. Z. Liao and J. S. Aitchison, "Precision etching for multi-level AlGaAs waveguides," *Opt. Mater. Express* 7(3), 895–903 (2017).
 58. W. D. Sacher, X. Luo, Y. Yang, F.-D. Chen, T. Lordello, J. C. C. Mak, X. Liu, T. Hu, T. Xue, P. Guo-Qiang Lo, M. L. Roukes, and J. K. S. Poon, "Visible-light silicon nitride waveguide devices and implantable neurophotonic probes on thinned 200 mm silicon wafers," *Opt Express* 27(26), 37400 (2019).
 59. B. J. Soller, D. K. Gifford, M. S. Wolfe, and M. E. Froggatt, "High resolution optical frequency domain reflectometry for characterization of components and assemblies," *Opt Express* 13(2), 666 (2005).
 60. J. F. Bauters, M. J. R. Heck, D. John, D. Dai, M.-C. Tien, J. S. Barton, A. Leinse, R. G. Heideman, D. J. Blumenthal, and J. E. Bowers, "Ultra-low-loss high-aspect-ratio Si₃N₄ waveguides," *Opt Express* 19(4), 3163 (2011).
 61. U. Glombitza and E. Brinkmeyer, "Coherent frequency-domain reflectometry for characterization of single-mode integrated-optical waveguides," *Journal of Lightwave Technology* 11(8), 1377–1384 (1993).
 62. J. Zou, Y. Yu, M. Ye, L. Liu, S. Deng, X. Xu, and X. Zhang, "Short and efficient mode-size converter designed by segmented-stepwise method," *Opt Lett* 39(21), 6273 (2014).